Experimental analysis of failure behaviour of PA12 specimens manufactured by SLS as a function of wall thickness and build direction

Alejandro Garcia Rodriguez
Facultad de Ingeniería Mecánica, Universidad Santo Tomás, Bogotá, Colombia and
Departamento de Ingeniería Mecánica y Mecatrónica, Universidad Nacional de Colombia, Bogotá, Colombia
Marco Antonio Velasco Peña
Facultad Tecnológica, Universidad Distrital Francisco José de Caldas, Bogotá, Colombia, and
Carlos A. Narváez-Tovar and Edgar Espejo Mora
Departamento de Ingeniería Mecánica y Mecatrónica, Universidad Nacional de Colombia, Bogotá, Colombia

Abstract

Purpose – This paper aims to investigate and explain the dual fracture behaviour of PA12 specimens sintered by selective laser sintering (SLS) as a function of wall thickness and build direction with a powder mixture 30:70. To achieve this objective, research related to chemical, thermal and structural behaviours as a function of the input variables was carried out to describe and explain why ductile-fragile behaviour occurs during fractures under uniaxial tension manufactured via a methodology of material analysis and manufacturing processes.

Design/methodology/approach – The factorial design 32 relates the fracture of PA12 tensile specimens to the horizontal, transverse and vertical build directions at 2.0, 2.5 and 3.0 mm thicknesses, respectively. Fractographic images revealed the fracture surfaces and their dual ductile-fragile behaviour related to the specimens' measured crystalline, thermal, surface and chemical properties.

Findings – The study showed that thermal property variables differ depending on the input variables. The wall thickness variable affected this morphology the most, showing the highest percentage of the ductile area, followed by the transverse and vertical directions. It was determined that the failure in the vertical direction is due to crystalline gradients associated with the layer-by-layer construction process. The pore density may be closely related to generating ductile and brittle areas.

Originality/value – In this paper, fracture characterisation is performed based on the mechanical, chemical, structural, thermal and morphological properties of PA12 manufactured by SLS. In addition, a heatmap of porosities in cross-sections is constructed using a machine learning model (k-means) related to dual fracture behaviour. This research revealed significant differences in the fracture type according to the build direction. In addition, thin-section fractography provides a more detailed explanation of the fragile behaviour of the vertical direction associated with crystalline changes due to the direction of the sintering layers.

Keywords Additive manufacturing, Selective laser sintering, Dual brittle-ductile fracture, Build direction, Wall thickness, Polyamide 12, Mixture 30 virgin, 70 recycled

Paper type Research paper

1. Introduction

Additive manufacturing is currently one of the most relevant research fields in engineering and science (Charoo, 2020; Yap, 2015; Olakanmi, 2013; Hejmady *et al.*, 2022). Its versatility allows it to be applied in biomedical, energy, automotive and aeronautical applications (Hashmi and Meena, 2023). There are many additive manufacturing processes, including selective laser sintering (SLS) (Cai, 2021; Balemans *et al.*, 2018; Van Hooreweder *et al.*, 2013). This technique allows the manufacture of nonparametric parts in production batches depending on the part size and amount of recycled material. Among the most commonly used materials is polyamide 12, a material with good mechanical strength (Martynková, 2021; Amado-Becker *et al.*, 2008).

Current research on this process focuses on defining, clarifying and establishing parameters for design guidelines applied to this type of additive manufacturing. However, some parameters related to the mechanical strength in these guidelines are general, and detailed information about the design thickness and mechanical properties is lacking as a function of the build direction (Materialise, 2024; Proto3000, 2024; 3D Systems, 2024). Research, such as Sasmita *et al.* (2019), Kelly (2019), Tasch *et al.* (2018), Fan (2021), Majewski and Hopkinson (2011), Jaksch *et al.* (2023) and Sindinger *et al.* (2020), have

The current issue and full text archive of this journal is available on Emerald Insight at: **https://www.emerald.com/insight/1355-2546.htm**

Rapid Prototyping Journal
30/8 (2024) 1537–1555

[DOI 10.1108/RPJ-01-2024-0038]

Received 27 January 2024
Revised 11 April 2024
Accepted 16 June 2024

shown that wall thickness and build direction significantly affect mechanical properties such as the ultimate tensile stress (UTS), elongation at break (Eab), elastic modulus (EM) and fracture type. Some of these investigations indicate that the parameters associated with breakage, including fracture type, exhibit random behaviour that cannot be fully explained.

Some authors have reported different fracture behaviours for PA12 manufactured by SLS. For example, Mehdipour *et al.* (2021) reported fragile behaviour and defects in the fractographies; however, spherulites remain in the fracture zone in all build directions. The authors observed an anisotropic behaviour and suggested that the fracture behaviour was due to poor interlayer fusion. The brittle behaviour of the entire fracture of the specimen fabricated by PA12 via SLS was also observed in the research of Liu *et al.* (2019). In contrast, Puttonen *et al.* (2021) reported the dual fracture behaviour of PA12 for the first time, with the specimens manufactured in the Z (vertical) and *x*-axis (horizontal) directions exhibiting brittle and ductile sections in the fracture zone. It is suggested that the fracture nucleated in the ductile zones, particularly in the spherulites of the material. In addition, the hypothesis that the fracture nucleates in the zones surrounding the surface defects was also proposed. During crack generation, ductile behaviour begins to appear and brittle behaviour predominates as the crack progresses (Amstutz *et al.*, 2021, 2022; Messiha *et al.*, 2022).

The existing research on dual fracture in Polyamide 12 by SLS is limited, and the fracture behaviour is not yet fully understood. Therefore, this study aims to develop a hypothesis that directly relates the mechanical, chemical, morphological, structural, thermal and morphological property criteria to clarify the fracture behaviour, which guides the failure analysis of this material.

Table 1 Combination table for the experimental design

N°	Condition	Buil direction	Wall thickness
1	H2	Horizontal	2.0
2	H2.5	Horizontal	2.5
3	H3	Horizontal	3.0
4	H2	Transverse	2.0
5	H2.5	Transverse	2.5
6	H3	Transverse	3.0
7	H2	Vertical	2.0
8	H2.5	Vertical	2.5
9	H3	Vertical	3.0

Source: Table by authors

2. Experimental approach

2.1 Experimental design

The experimental design was a 3^2 three-level full factorial design (Douglas, 2001) with two factors or independent variables: build direction and wall thickness. Each factor has three levels: vertical, horizontal and transverse build directions, as well as wall thicknesses of 2.0, 2.5 and 3.0 mm, respectively. Table 1 shows the combinations for each factor and level.

The number of replicates was calculated with $\beta = 0.09$, $\alpha = 0.05$ and an expected standard deviation of 0.6 MPa for eight replicates per combination. A total of 72 tension tests were performed on the manufactured specimens. A total of 432 specimens were manufactured, with 48 specimens per condition. The specimens were numbered for each condition; eight were randomly selected for tensile testing, while one was randomly chosen from the remaining 40 specimens for the chemical, structural and thermal tests.

Uniaxial tensile specimens were fabricated on a commercial EOS Formiga P110 Velocid machine with the manufacturer's recommended criteria following ISO 257-Type I guidelines. The samples were manufactured with a CO_2 laser power of 30 W, a scan speed of 5 m/s, a layer thickness of 0.12 mm and a build rate of 1.21/h. An EOS PA12 mixture of virgin and recycled powder (30:70) was used, and the scanning strategy of the machine was predetermined. This mixture is used commercially to manufacture parts, but it is not frequently

Figure 1 Boxplot of the XRD curves

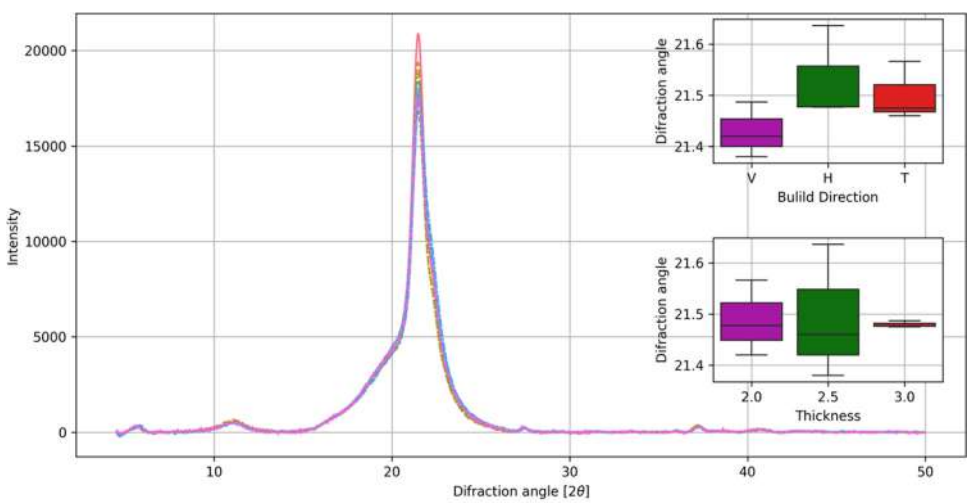

Notes: The mean diffraction angle is a function of the build direction and thickness
Source: Figure by authors'

reported in the literature, so it is necessary to provide fracture criteria to users to improve the failure analysis of components manufactured by SLS.

2.2 Statistical analysis

The Anderson–Darling and Levene tests were used to evaluate the assumptions of normality and homoscedasticity. ANOVA tests were applied to assess significant differences. A q-norm transformation was used to determine the normality of the data.

Table 2 ANOVA associated with the diffraction angles of the alpha phase

Factor	Normality	Homoscedastic	F value	*p*-value
Diffraction angle	*0.166*	*0.927*	BD: 1.65 Th: *0.016*	BD: *0.268* Th: *0.984*

Notes: T-H is the transverse vs horizontal direction; V-H is the vertical vs horizontal direction; V-T is the vertical vs transverse direction. BD is the building direction, and Th is the thickness. *Significant differences; **Very significant differences
Source: Table by authors

Due to the number of replicates, the stress tests evaluate the interaction between variables, while the difference between means is only evaluated in the structural and thermal characterisations. The characteristics of the mechanical properties were developed in Garcia *et al.* (2023).

2.3 Spectroscopy infrared spectroscopy

Infrared spectroscopy (FT-IR) spectra were obtained using a Shimadzu IRAffinity-1S spectrophotometer using the attenuated total reflection technique. The measurement conditions were a spectral resolution of 8 cm^{-1}, 64 scans per spectrum and a wavenumber range between 200 and 400 cm^{-1}.

2.4 X-ray diffraction

The powder crystalline structure was determined using a Philips diffractometer with a 30 kV voltage and 20 mA current, operated in the Bragg–Brentano configuration with K alpha signals from the copper anode ($\gamma = 0.1542$ nm), between 2Θ values of 5°–50° and a step of 0.02°.

Table 3 Diffraction angle as a function of build direction and thickness compared to related research

Phase	Build direction	Thickness (mm)	Present investigation (°)	Yao *et al.* (2020)	Cai *et al.* (2021)	El Magri *et al.* (2022)	Rosso *et al.* (2020)	Van Hooreweder *et al.* (2010)
Gamma	V	2.0	V2.0 → 21.42	21.3	21.2	21.0	21.0	21.2
	V	2.5	V2.5 → 21.38					
	V	3.0	V3.0 → 21.49					
	H	2.0	H2.0 → 21.48					
	H	2.5	H2.5–21.64					
	H	3.0	H3.0–21.48					
	T	2.0	T2.0–21.57					
	T	2.5	T2.5–21.46					
	T	3.0	T3.0–21.47					

Source: Table by authors

Figure 2 Infrared spectrum of specimens as a function of the build direction and wall thickness of PA12 through SLS

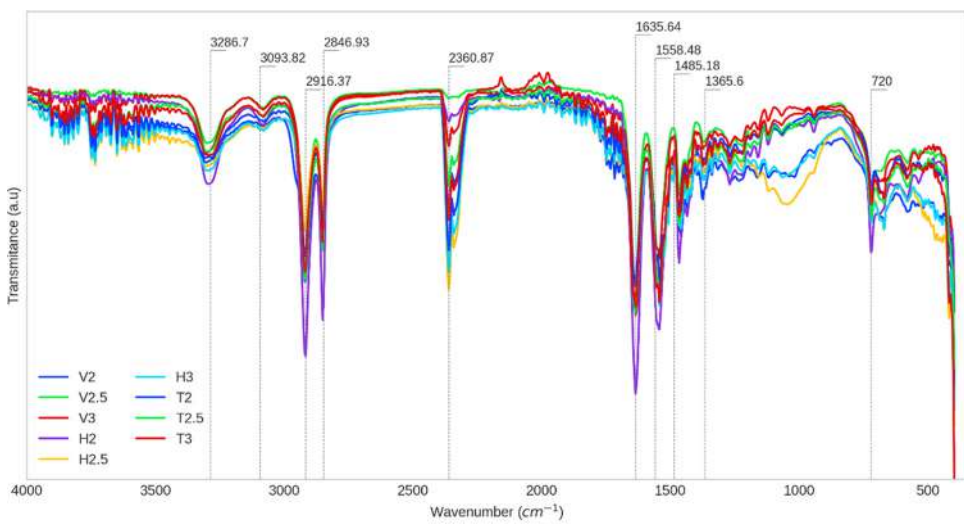

Source: Figure by authors'

2.5 Scanning electronic microscopy

The fracture of the specimens and surface morphology were determined using SEM on a Vega 3 Tescan instrument operated at 15 kV and 10 mA with a gold metallised specimen.

2.6 Calorimetry differential scanning

A Mettler Toledo differential scanning calorimeter (1–500/227) was used for thermal characterisation. The temperature range was between 25°C and 200°C with a heating and cooling rate of 10°C/min in a N_2 atmosphere. The fusion

Table 4 FTIR functional groups of the PA12 specimens manufactured by SLS

Functional group	Present investigation (cm^{-1})	Cai *et al.* (2021) (cm^{-1})	Martynková *et al.* (2021) (cm^{-1})	Yu *et al.* (2022) (cm^{-1})	Ma *et al.* (2020) (Ning, 2020) (cm^{-1})
N-H Stretching	3,286.7	3,292	3,290	3,295	3,298
N-H Stretching	3,093	–	3,094	3,076	3,098
CH2 Stretching	2,846	2,846	2,916	–	–
Amide I Stretching	1,654	1,637	1,638	–	–
Amide II Bending	1,578	1,558	1,561	1,533	1,557
CH2 Scissoring	1,485	1,458	1,459	–	–
CH2 Twisting	1,365	1,367	1,368	–	–
Amide III Stretching	1,275	1,269	1,268	–	–
CO–NH	–	1,159	1,159	–	–
CO–NH	–	1,120	1,062	–	–
CO–NH Bending	962	949	948	–	–
CH2 Rocking	720	710	721	–	–
AmidE IV Bending	632	–	621	678	626

Source: Table by authors

Figure 3 (A) Exothermic curves of specimens of PA12 (B) Endothermic curves of specimens of PA12 (C) Crystallinity distribution as a function of build direction (D) Crystallinity distribution as a function of thickness

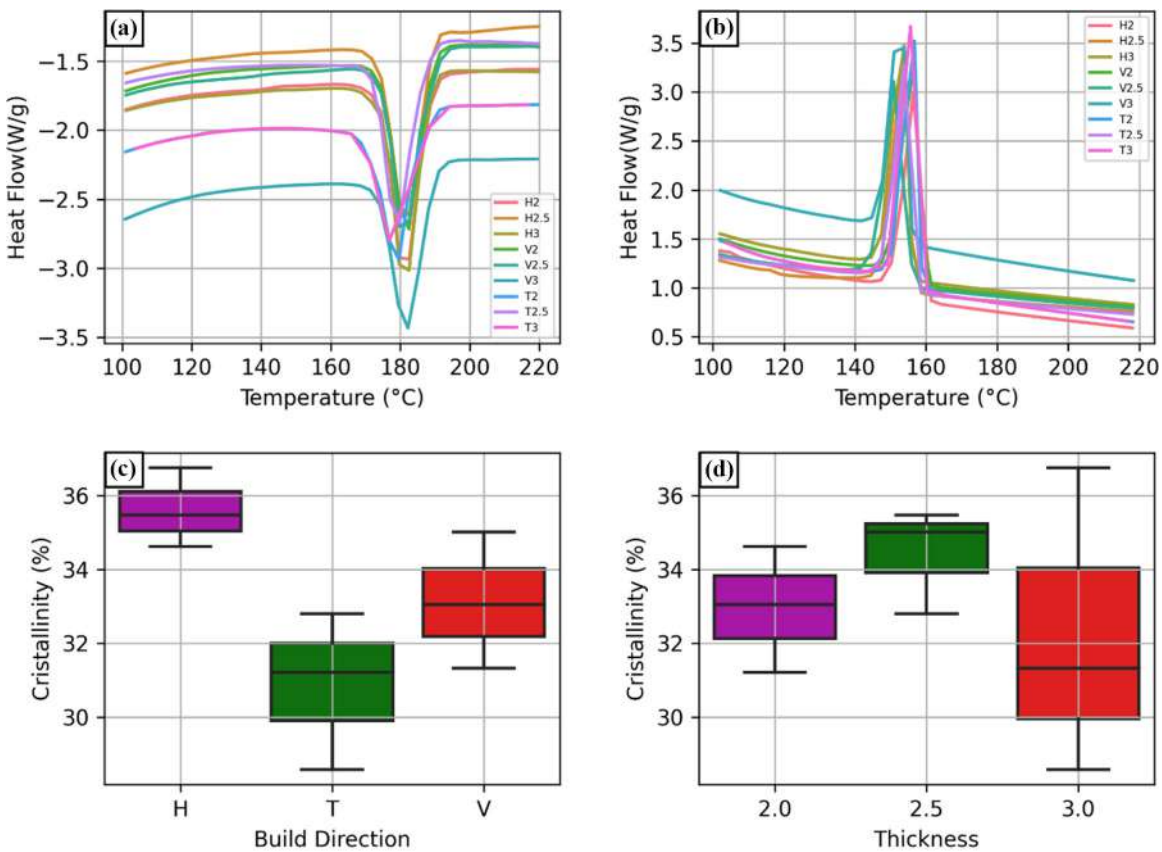

Source: Figure by authors'

enthalpy and crystallinity percentage were calculated using Origin Pro software.

2.7 Surface rougness

Surface roughness was measured using a Zeiss LSM 700 confocal laser microscope with a 100X lens and 455 nm laser, and a PinHole with an Aury unit opening was used. The surface roughness was measured on the side of the specimen where the marks associated with the build direction and the wall thickness were present.

2.8 Thin cutting microtome

The crystallinity of the specimens was observed under a Carll Zeiss polarised transmitted light microscope. A wave polariser with a quarter-wave retarder was used. A Microtome with macro search HP35 high-profile blades was used for sample

Table 5 Thermal properties, namely, the crystallisation temperature (Tc), melting temperature (Tm) and crystallinity (PC), of specimens manufactured in PA12 by SLS

	Present research			Tasch *et al.* (2018)			Ferreira *et al.* (2020)		
Combination	**Tc (°C)**	**Tm (°C)**	**PC (%)**	**Tc (°C)**	**Tm (°C)**	**PC (%)**	**Tc (°C)**	**Tm (°C)**	**PC (%)**
V 2.0	182.51	156.68	33.042	–	–	0.6 mm- 35	–	176.3.5	16.9
V 2.5	179.78	150.88	35.006			0.8 mm- 33			
V 3.0	182.23	153.66	31.320			28.3 mm- 36			
H 2.0	182.61	156.41	34.619			2.0 mm- 32			
H 2.5	182.64	153.79	35.467			4.0 mm- 31			
H 3.0	182.53	153.73	36.753						
T 2.0	179.63	156.73	31.210						
T 2.5	179.84	153.68	32.801						
T 3.0	176.87	155.61	28.578						

Source: Table by authors

Table 6 ANOVA associated with the crystallinity percentage

Factor	**Normality**	**Homoscedastic**	**F Value**	***p*-value**	**Post hoc**
PC	*0.85*	*0.72*	*5.58*	BD: *0.043***	T vs H → 4.7 e^{-03} **
				Th: *0.624*	V vs H → *0.40*
					V vs T → 0.50

Notes: T-H is the transverse vs horizontal direction; V-H is the vertical vs horizontal direction; and V-T is the vertical vs transverse direction; *Significant differences. **Very significant differences
Source: Table by authors

Figure 4 (A) Surface of specimen manufactured by SLS. (B) The presence of particles near the fracture site of PA12

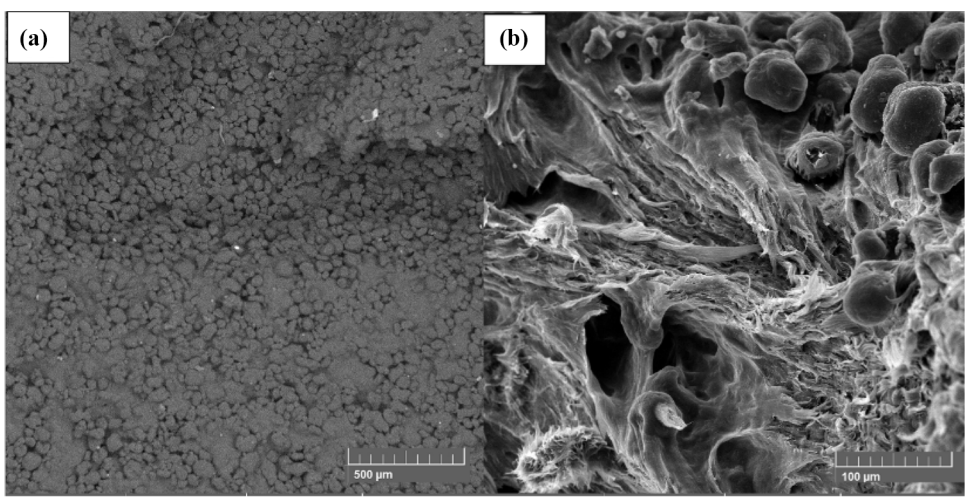

Source: Figure by authors'

cutting. Samples of 10 μm thick specimens were taken from specimens in the fracture zone.

2.9 Porosity heatmap

Porosity images were obtained via cross-sectional microtomography. The heatmap was created using the Python program with the OpenCV library. The k-means classification machine learning algorithm from the Sckit Learn library was used for cluster placement in the heatmap with a value of 50 clusters. This map was generated with artificial intelligence-created contour lines associated with defect density and diameter, showing a tendency for porosity in cross-sections of the specimen.

Table 7 Surface and areal roughness as a function of build direction and wall thickness

Build direction	Wall thickness (mm)	Sa (μm)	SD (μm)	Petzold *et al.* (2019) (μm)	Varotsis *et al.* (2021) (V. A., 2024) (μm)
Vertical	2.0	19.9	1.03	20.0–26.5	3.2–18
	2.5	20.7	0.34		
	3.0	20.7	0.71		
Horizontal	2.0	19.6	1.39		
	2.5	21.0	0.63		
	3.0	20.7	1.28		
Transverse	2.0	20.0	1.28		
	2.5	21.3	0.76		
	3.0	20.8	0.53		

Source: Table by authors

Figure 5 The data distribution is a function of the build direction and wall thickness of the PA12 specimens

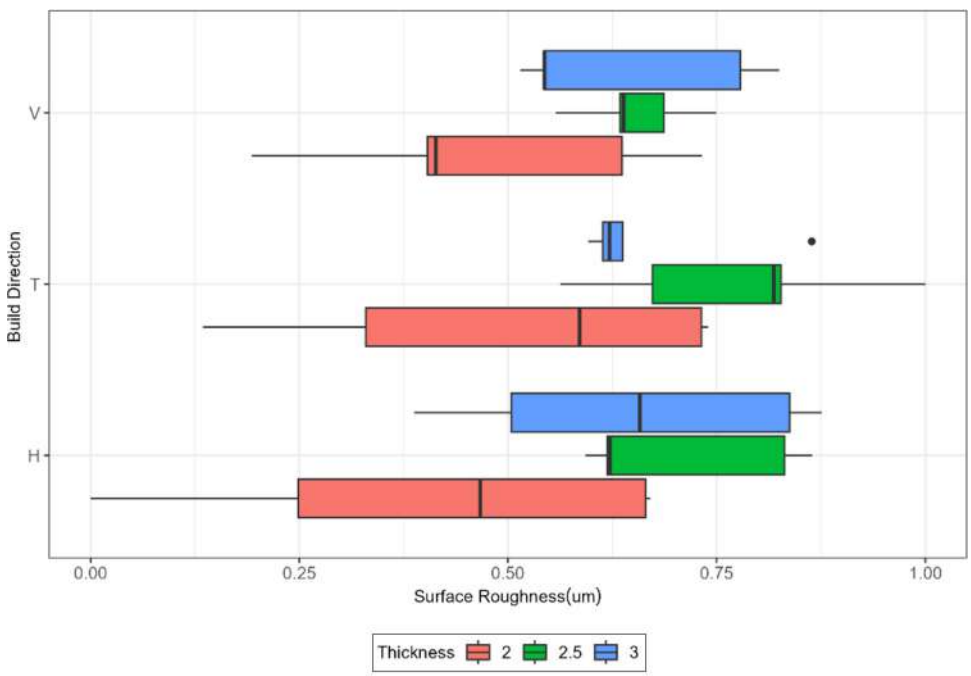

Source: Figure by authors'

Table 8 ANOVA of the surface roughness of PA12 manufactured by SLS

			F and *p*-values of the ANOVA test		
Factor	**Normality**	**Homoscedastic**	**F Value**	***p*-value**	**Post hoc**
Surface roughness	*0.29*	*0.38*	BD: 0.537	BD: *0.589*	2.0 vs 2.5 → $9.7\,e^{-05**}$
			Th: 7.415	Th: *0.002****	2.0 vs 3.0 → $1.7\,e^{-03**}$
			Th:BD: 0.199	Bd:Th: 0.937	2.5 vs 3.0 → 1.0

Notes: T-H is the transverse vs horizontal direction; V-H is the vertical vs horizontal direction; and V-T is the vertical vs transverse direction; *Significant differences. **Very significant differences

Source: Table by authors

3. Results

3.1 X-ray diffraction

Figure 1 shows the diffractogram of the specimens manufactured by SLS, which shows an average diffraction angle of 21.49° associated with the gamma phase of the material (Martynková, 2021; El Magri *et al.*, 2022). The gamma phase is generated under rapidly cooled polyamide 12 (Salmoria *et al.*, 2009; Hiramatsu *et al.*, 1983). The laser passes through the powder during sintering, and point heating rapidly cools the sintered section. This sintering process generates a left

Figure 6 Strain stress curves

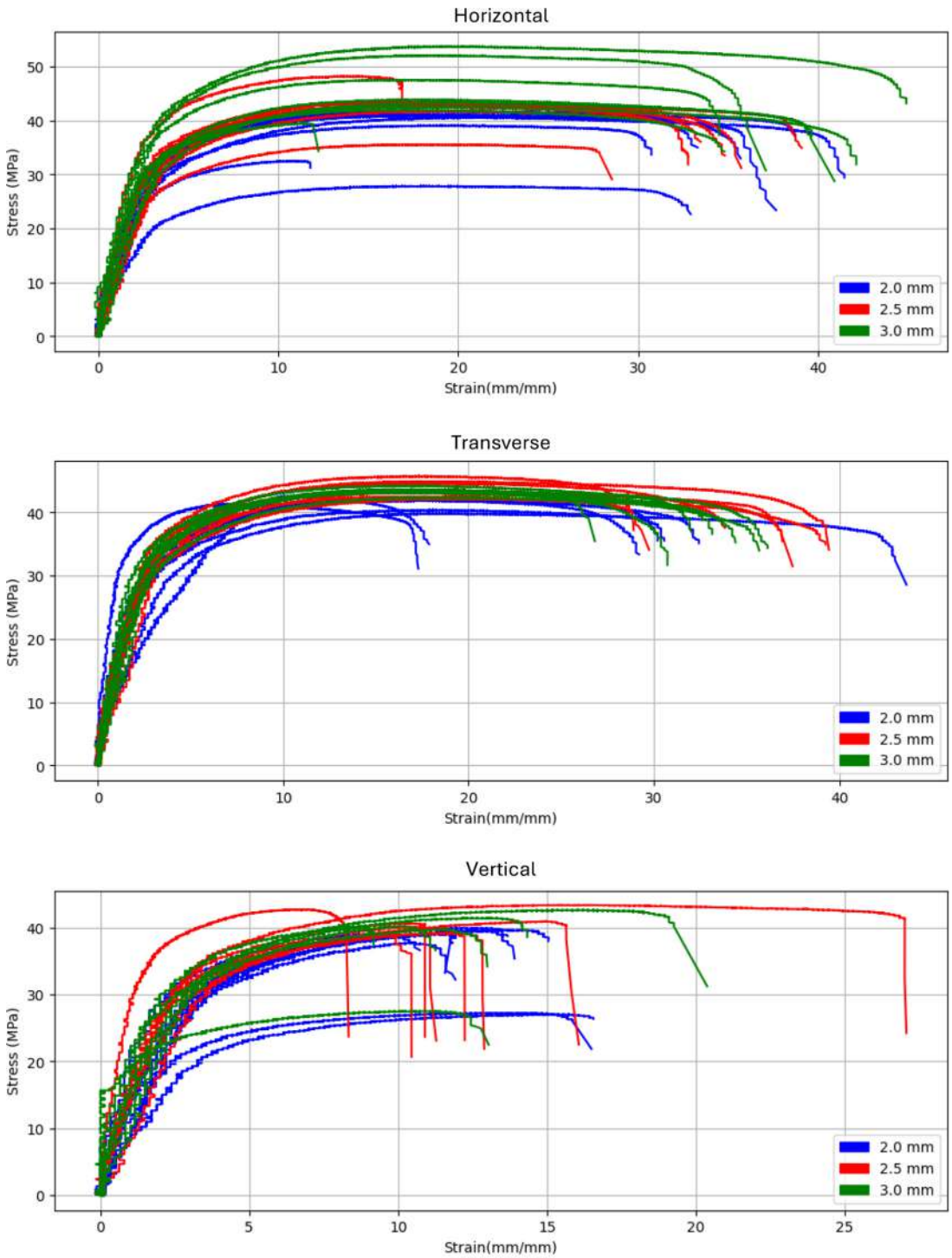

Notes: (A) Horizontal direction; (B) transverse direction; (C) vertical direction
Source: Figure by authors'

shoulder in the gamma phase spectrum, corresponding to the remaining section of the alpha phase.

The angle distributions of the gamma signal as a function of wall thickness and build direction are shown in Figure 1 in boxplot graphs. According to the ANOVA test (Table 2), the build direction and wall thickness did not affect the angle associated with the gamma phase.

Table 3 compares the average angle of each condition with those reported in some relevant papers. Similar behaviour was observed for the mean value, indicating that even though the powder is sintered under different machine parameters, mixing, directions or thicknesses, its angle tends to remain close to 21°.

3.2 Infrared transform fourier

Figure 2 shows the IR spectra associated with the specimens as a function of their build direction and wall thickness. The signals associated with amide I (1654 cm^{-1}), amide II (1578 cm^{-1}), amide III (1275 cm^{-1}) and amide IV (632 cm^{-1}) groups can be distinguished (Hejmady *et al.*, 2022).

Table 4 shows some related research on the composition of nylon PA 12. Most studies show the same amide groups as the present study, but some signals, such as those of amides I and II, are weak. This difference in behaviour could be attributed to differences in powder mixing, sample preparation and equipment conditions.

3.3 Differential scanning calorimetry

Figure 3 shows the thermal behaviour of the specimens manufactured by the SLS. Figure 3(a) shows the exothermic curves, and Figure 3(b) shows the endothermic curves of the specimens. Shifts in the curves are observed under some conditions, indicating that the melting and crystallisation temperatures changed.

The values associated with crystallisation temperatures, melting temperatures and crystallisation percentage are shown in Table 5. The melting and crystallisation temperatures are inversely proportional to the wall thickness. The melting temperature per building direction was 181.5°C in the vertical direction, 178.78°C in the transverse direction and 181.54°C in the horizontal direction. The average crystallisation temperatures obtained were 153.74°C, 155.34°C and 153.65°C for the vertical, transverse and horizontal building directions, respectively.

Figure 3(c)–(d) shows a boxplot of the percentage of crystallinity. ANOVA revealed a significant difference between the horizontal and transverse directions (Table 6). The horizontal direction presents a higher percentage of crystallinity, which could be associated with the higher sintering surface layer with a lower cooling rate, which suffers a kind of intrinsic annealing during the process.

Although the percentage of crystallinity did not show significance as a function of wall thickness, it was observed in all directions that the mean value increased from 2.0 to 2.5 mm thicknesses, followed by a drop at 3.0 mm. The decrease in the average crystallinity percentage at a thickness of 3.0 mm suggested that the cooling time was insufficient for a large portion of the mass to crystallise, resulting in a more significant amorphous zone. This behaviour of the crystallinity percentage as a function of thickness has been observed in other studies,

Figure 7 Fractured specimens after tensile testing in the (A) horizontal direction, (B) transverse direction and (C) vertical direction

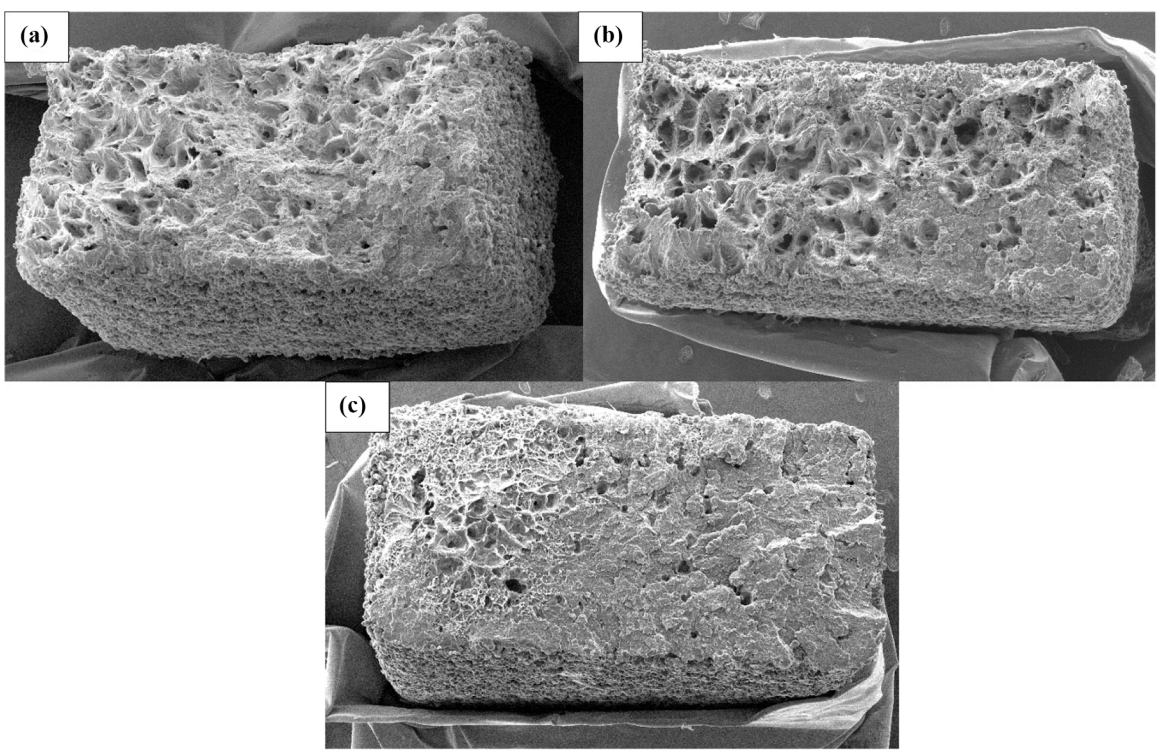

Source: Figure by authors'

such as that of Tasch *et al.* (2018) and Sindinger *et al.* (2020), who reported that the average crystallinity percentage tends to decrease as the wall thickness increases.

3.4 Surface roughness

Figure 4. shows a partial fusion of particles on the surface of the specimens. These partially fused particles are possibly a product of the remaining heat in the last sintering layers. These particles were also observed in the fracture zones of the specimens, possibly as crack nucleators, as was reported by Caulfield *et al.* (2007) and Khan *et al.* (2021).

Table 7 shows the surface roughness values of the specimens, with average values varying between 20 and 22 μm. The thickness of 2.0 mm presents the lowest value in all build directions. The roughness increases vertically by 3.86%, decreases by 1.44% in the transverse direction and decreases by 5.32% in the horizontal direction. The roughness values do not have a wide range because the roughness depends mainly on the combination of powder and laser parameters (Wolf *et al.*, 2020). Accordingly, the roughness values are close in the same batch under mixing conditions and laser parameters.

Figure 5 evaluates the distribution of surface roughness data for each of the conditions. The variation between the ranges is

Figure 8 Fractography

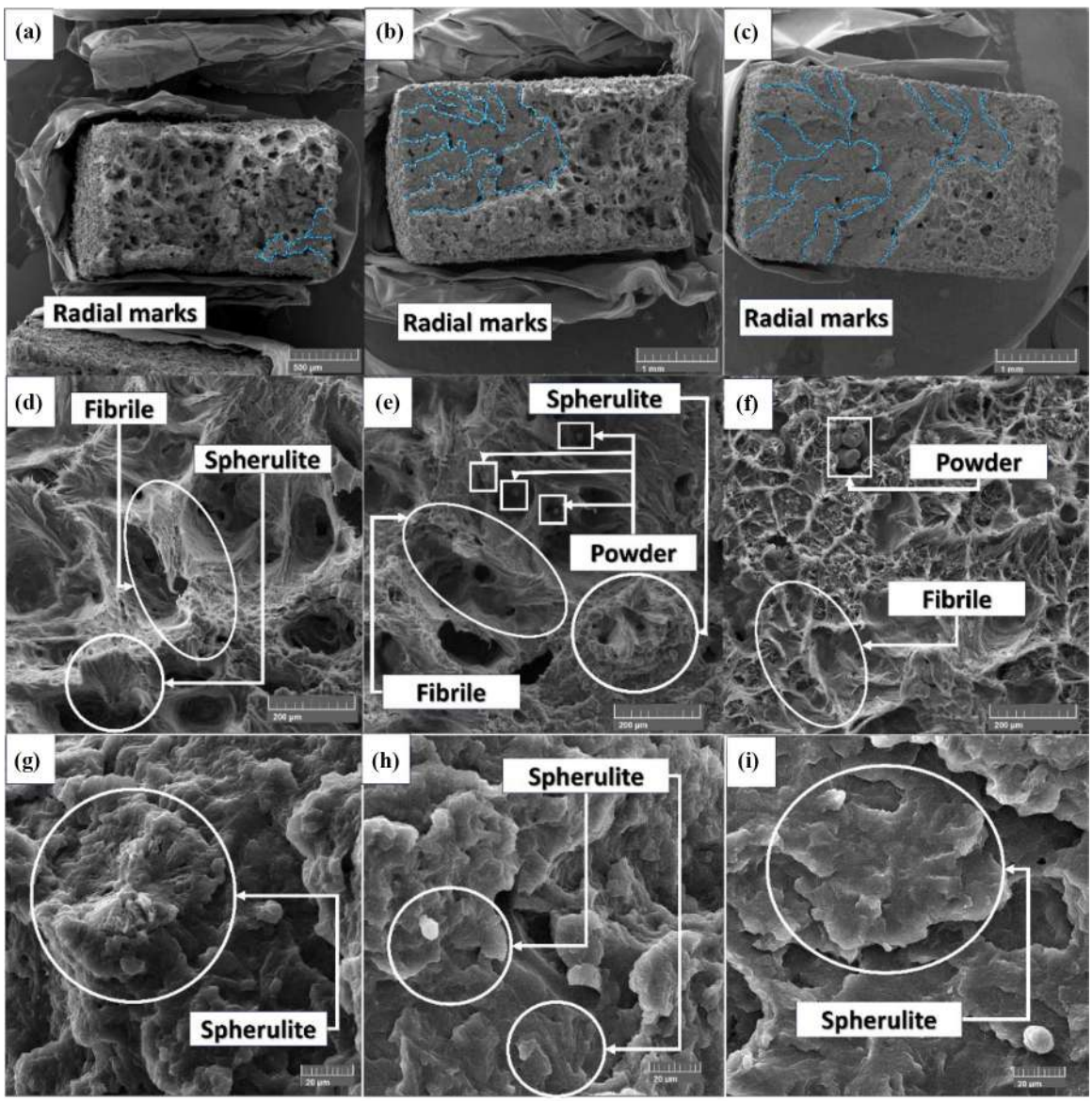

Notes: (A) Horizontal direction; (B) transverse direction; (C) vertical direction. Fractography of the ductile zone; (D) horizontal direction; (E) transverse direction; (F) vertical direction. Fractography of the fragile zone; (G) horizontal direction; (H) transverse direction; (I) vertical direction
Source: Figure by authors'

considerable. This behaviour could be associated with the thermal gradients in the sintering chamber. Nelson and Rennie (2015) showed that thermal differences depending on the location of the part in the powder bed can influence the mechanical and surface properties.

The ANOVA of the surface roughness (Table 8) showed significant differences at a thickness of 2.0 mm, with the lowest value compared to the other conditions. This behaviour is associated with the fact that these specimens presented the lowest mass, and therefore, their cooling was possibly faster, causing a better fusion of particles on the surface.

3.5 Stress–strain curves

Figure 6 shows the stress–strain curves of the specimens manufactured by SLS. The specimens manufactured in the horizontal direction exhibited the highest ductility and UTS, followed by those manufactured in the transverse direction. These two directions present more ductile behaviour than the vertical direction, representing values lower than 25% of the deformation and the lowest mechanical resistance. In addition, as the thickness increased, the ductility and UTS tended to increase in all directions. The values and statistical significance of the mechanical properties are mentioned in the following publication (Garcia *et al.*, 2023).

3.6 Fracture study

The fracture morphology showed a flat region with radial marks associated with the sudden-fragile fracture process and a region with microvoids related to the sudden-ductile fracture process (Figure 7).

The behaviour of the specimens manufactured in the horizontal direction [Figure 8(a)] showed high percentages of ductile zones on the fracture surface. The radial marks coming from the polymer surface (blue marks) are shown in the brittle fracture zone. Compared with those in the horizontal direction, the area and number of radial marks in the brittle fracture zone associated with the specimens fabricated in the transverse direction [Figure 8(b)] increased. The fractures of the specimens in the vertical direction [Figure 8(c)] exhibited more brittle behaviour than those in the other two directions. The fibrils associated with the ductile zone in the vertical direction were much shallower than those in the other build directions.

The ductile fracture zone concerning the build direction [Figure 8(d)–(f)] revealed fibrils surrounding the microvoids with partially fused particles, and fractured spherulites were identified in the ductile zone. The brittle fracture zone concerning the build directions [Figure 8(g)–(i)] showed more homogeneous behaviour than the ductile zone; spherulites were observed along the fracture zone in all directions, and no fibrils were observed in the fractures of the manufactured specimens.

Figure 9 shows a spherulite crystal with deformations in the ductile zone of the fracture. These behaviours (Figures 8 and 9) suggest that the spherulites underwent a deformation process related to generating fibrils. In those build directions with a high percentage of ductile fracture, a lower percentage of transversally fractured spherulites was observed (fragile zone). This behaviour indicates that the material undergoes a high degree of sintering in this direction, so the correctly fused spherulites are deformed into fibrils when the load is applied to the specimen.

Figure 9 (A) Deformed spherulites in a matrix of fibrils (B) partially deformed spherulites

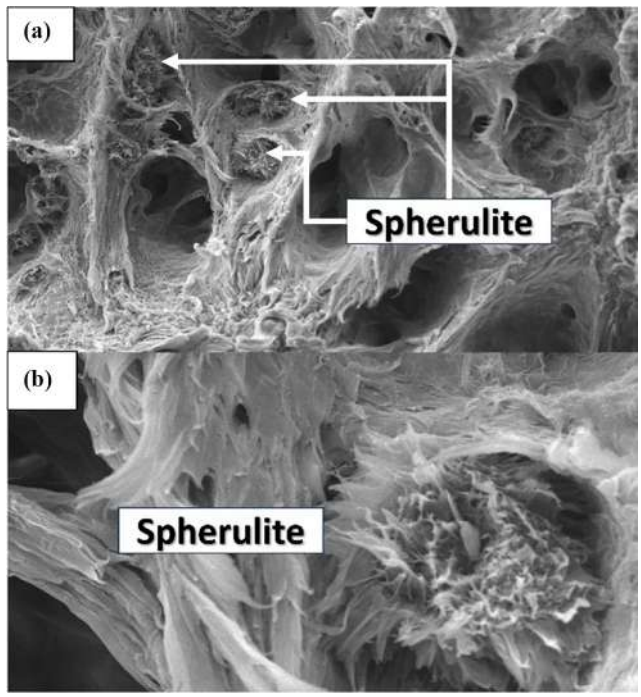

Source: Figure by authors'

Table 9 shows that the percentage of the fracture ductile zone increased by 3.05% and 6.4% for thicknesses of 2.5 and 3.0 mm, respectively, compared to the thickness of 2.0 mm in the vertical direction. In the horizontal direction, there was a difference of 12.9% and 17.6%, while in the transverse direction, values of 2.5% and 19.4% were observed for the 2.5 and 3.0 mm thicknesses, respectively, compared to the thickness of 2.0 mm. The standard deviation was greatest in the transverse direction, indicating that this direction had the most significant percentage change.

Figure 10 shows the data distribution of the percentage of ductile fracture in the specimens as a function of the build direction and wall thickness. The data show a pattern as a function of thickness, with lesser thicknesses representing a more significant amount of ductile fracture zone. On the other hand, the fractures that presented the highest percentage of

Table 9 Mean values and standard deviation (SD) of the fracture ductile zone of specimens as a function of the build direction and wall thickness

Build direction	Wall thickness (mm)	Ductile Fracture (%)	SD
Vertical	2.0	27.6	3.74
	2.5	28.6	2.90
	3.0	29.5	3.74
Horizontal	2.0	55.4	12.8
	2.5	58.6	14.0
	3.0	67.3	8.46
Transverse	2.0	46.7	22.7
	2.5	59.5	23.3
	3.0	58.0	5.72

Source: Table by authors

Figure 10 Boxplot of the percentage of ductile fracture in the specimens manufactured by SLS as a function of the build direction and thickness of the wall

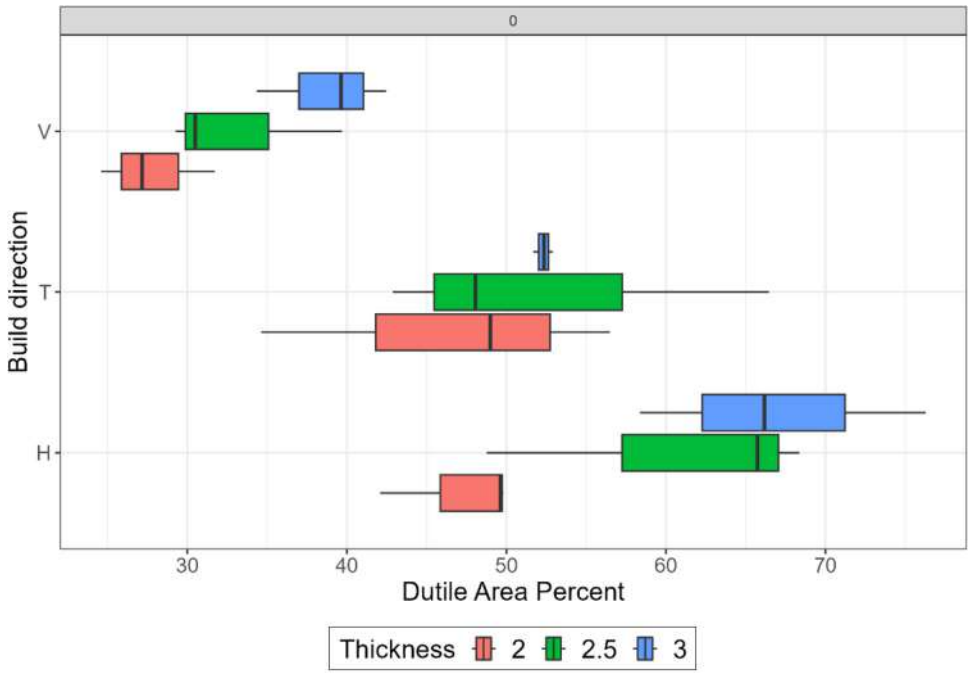

Source: Figure by authors'

ductility were in the horizontal, transverse, and vertical directions. The ranges vary significantly, particularly in the T2.5 direction, associated with excessive ductility.

According to ANOVA, significant differences in the percentage of ductile fracture were found, mainly associated with the build direction (Table 10). Post hoc tests revealed significant differences between the vertical transverse and horizontal directions.

The sintering construction layers were observed only in the micrographs of the specimens manufactured in the vertical direction [Figure 11(a)–(b)], suggesting an anisotropy in the crystalline condition in the specimen cross-section related to the build direction. The build layers presented a hue intensity pattern possibly associated with crystalline changes between the sintering layers, reflecting nonuniform melting in the cross-sectional area of the specimen, which could explain the low elongation percentage in the strain stress curves (Figure 6). This morphological characteristic was not observed in the horizontal [Figure 11(c)–(d)] or transverse [Figure 11(e)–(f)] directions, which presented the most significant differences in Eab as a function of build direction.

The fracture was characterised by thin sections (10 μm) obtained by microtomy. The specimens manufactured in the vertical direction (Figure 12) exhibited a fracture zone parallel to the sintering layers (Figure 10), and cracks were observed near the fracture zone. Cracks occurred in the amorphous and crystalline zones through spherulites in a transverse manner.

The fracture in the specimens manufactured in the transverse direction (Figure 13) showed ductile deformation with fibrils and an irregular shape of the fracture surface, which may be associated with the loading not being in the same direction as the build of the specimen. The presence of fibrils in the fracture may be related to the correct fusion between the layers of the specimen, which explains why the fusion between layers was lower in the vertical direction.

Fractures in the specimens manufactured in the horizontal direction (Figure 14) exhibited more ductile behaviour than those in the other two directions, which is reflected in their morphology, which has a greater number of fibrils and deformed zones and the irregular shape of the fracture is more chaotic than that corresponding to the transverse direction.In the fracture zone, two behaviours related to the quality of the sintering process were observed between sections. The first behaviour [Figure 15(a)–(b)] shows partially sintered particles in the fracture zone. These particles are located on the outer surface of the specimen, showing radial crystalline patterns. The second behaviour [Figure 15(c)–(d)] is characterised by more homogeneous radial spherulites associated with a correct sintering process. These behaviours and the radial markings of the fracture surface suggest that the crack is nucleated from the most anisotropic crystalline point at the surface.

3.7 Porosity

Figure 16 shows the heatmap as a function of the pore location and diameter in the specimen cross-section as a function of the build direction and part thickness. A random behaviour is observed in the distribution of the pores. However, it was shown that the tendency of accumulation is in the centre and on the periphery of the cross-section. This behaviour, together with the radial marks of the specimens, would indicate a concentration of stresses in surrounding areas on the surface, which would have repercussions on the nucleation of the fracture from the surface of the specimen.

Table 10 ANOVA of ductile fracture sections of PA12 manufactured by SLS

Factor	Normality	Homoscedastic	F and *p* values of the ANOVA test F Value	*p*-value	Post hoc
% Ductile fracture	*0.196*	*0.08*	BD: *23.059* Th: *2.577* *BD-Th:0.393*	BD: *8.6 e-*^{06**} Th: *0.315* *BD-Th:0.679*	Build direction T vs H → 0.86 V vs H → 1.1 e $^{-06*}$ V vs T → 2.8 e $^{-05*}$

Notes: T-H is the transverse vs horizontal direction, V-H is the vertical vs horizontal direction and V-T is the vertical vs transverse direction *Significant differences **Very significant differences
Source: Table by authors

Figure 11 Thin section of the longitudinal section observed by (I) polarised microscopy (II) polarised microscopy with quarter-wave retardation

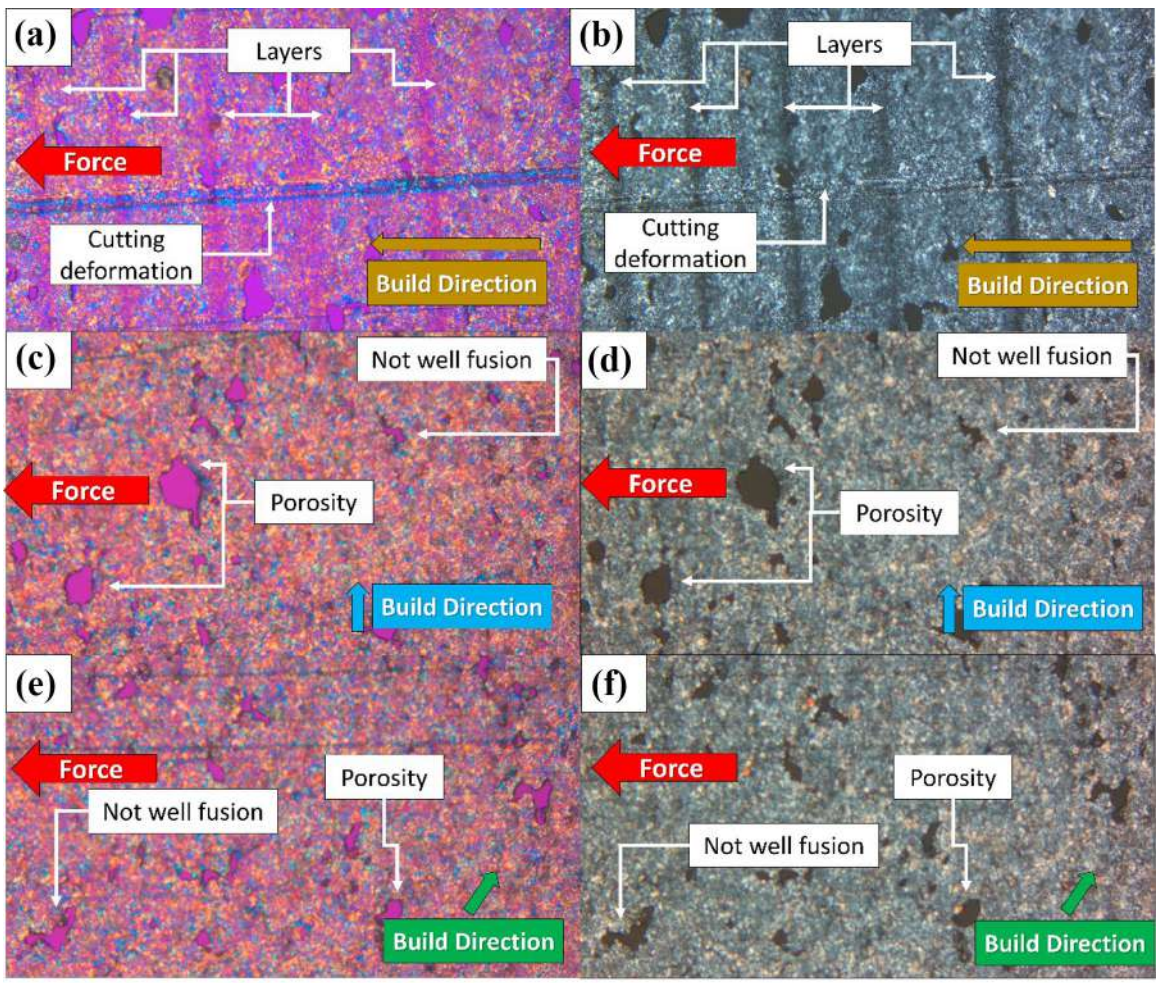

Notes: (A) Vertical direction; (B) transverse direction; (C) horizontal direction
Source: Figure by authors'

3.8 Behaviour of specimens

The behaviour of the specimens as a function of the build direction and thickness is shown in Figure 17. The mechanical behaviour in the vertical direction tends to remain constant. However, the pore diameter, cross-section and percentage of ductile fracture present the most marked changes. However, the pore diameter, cross-section and percentage of ductile fracture present the most significant changes. Figure 17(a) shows the transverse direction, which has different behaviours in terms of mechanical properties. However, the variables that show changes are the same as those in the transverse section except for the Eab. Finally, there is a more significant change in the ductile fracture in the vertical direction [Figure 17(c)].

Figure 12 Thin section of fracture morphology in the vertical direction

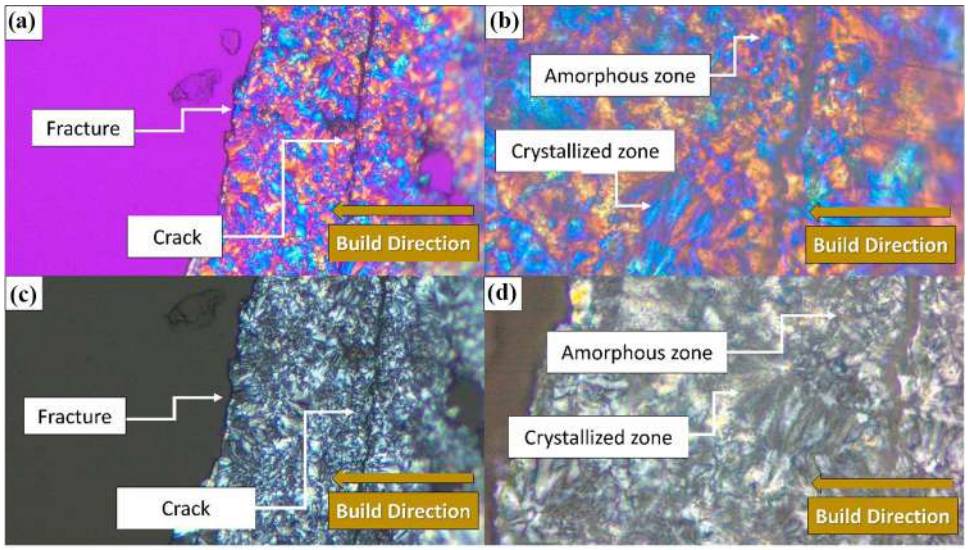

Notes: (A) Polarised microscopy, 200X; (B) polarised microscopy with quarter-wave retardation, 200X. (C) Polarised microscopy, 500X; (D) polarised microscopy with quarter-wave retardation, 500X
Source: Figure by authors'

Figure 13 Thin section of fracture morphology in the transverse direction

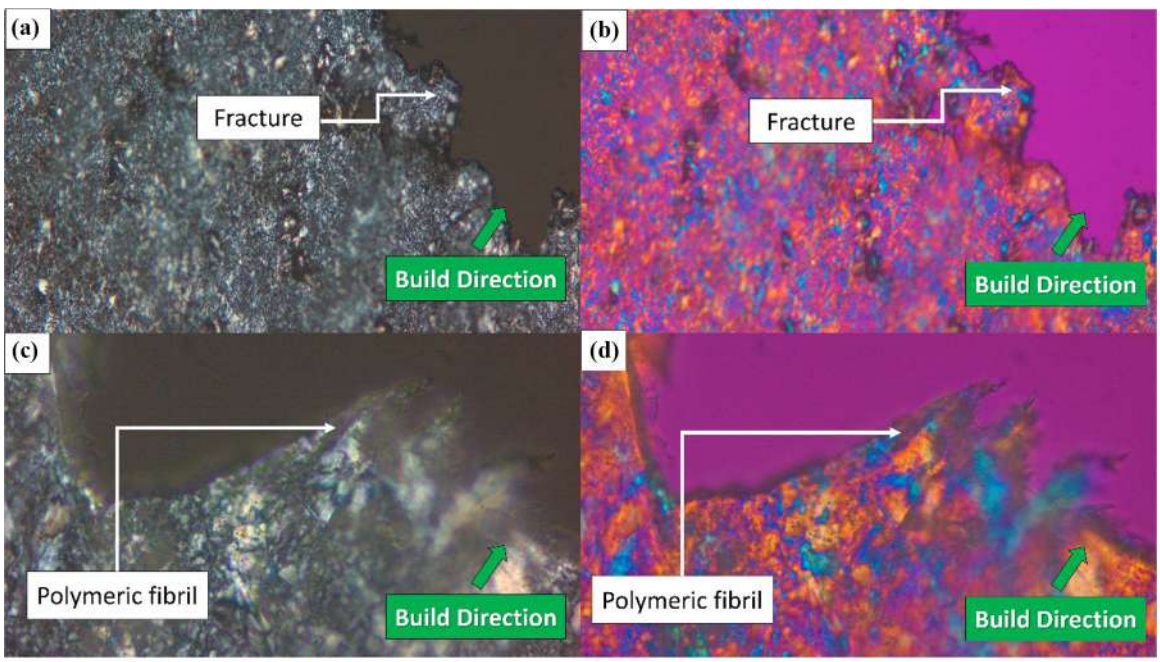

Notes: (A) Polarised microscopy, 200X; (B) polarised microscopy with quarter-wave retardation, 200X; (C) Polarised microscopy, 500X; (D) polarised microscopy with quarter-wave retardation, 500X
Source: Figure by authors'

4. Discussion

XRD and FTIR analyses, which examined the structure and chemical composition, showed that the functional groups and diffraction angle did not exhibit any notable changes concerning the build direction or wall thickness. Hence, it can be inferred that these factors do not impact the dual fracture behaviour.

According to the thermal DSC analysis results, the percentage of crystallinity in the samples varied based on the

Figure 14 Thin section of fracture morphology in the horizontal direction

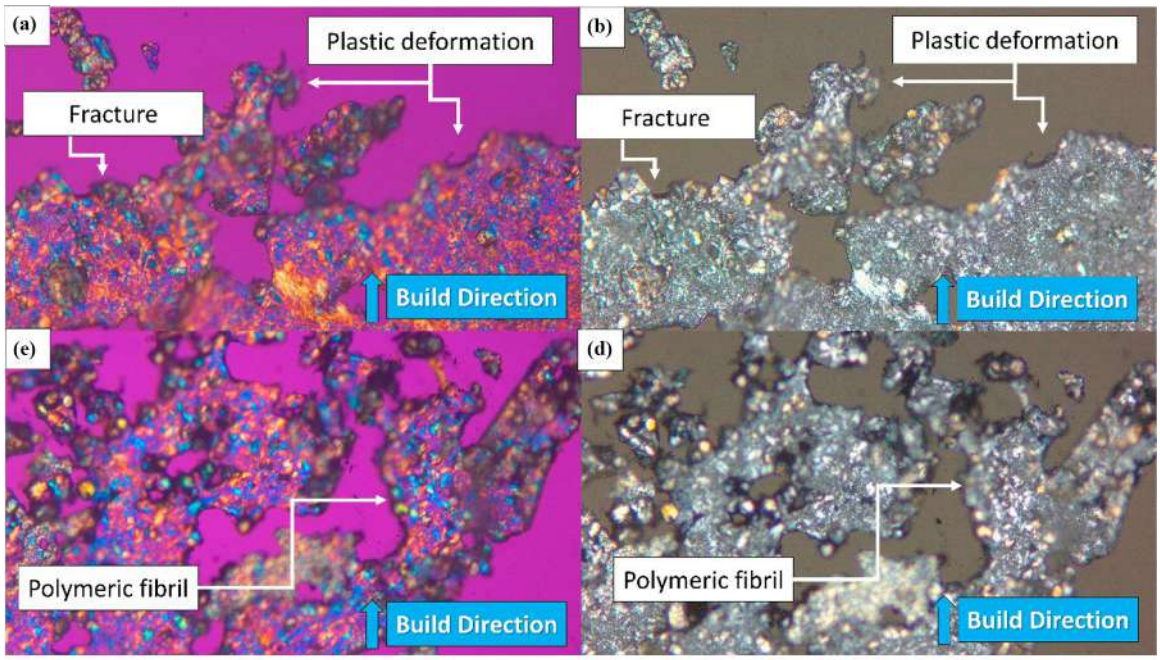

Notes: (A) Polarised microscopy, 200X; (B) polarised microscopy with quarter-wave retardation, 200X; (C) Polarised microscopy, 500X; (D) polarised microscopy with quarter-wave retardation, 500X
Source: Figure by authors'

Figure 15 Thin section of the longitudinal section observed by (B, D, F) polarised microscopy, (A, C, E) polarised microscopy with quarter-wave retardation and (A, B) fracture with the presence of partially fused particles. (C, D) Fusion of particles in the failure zone

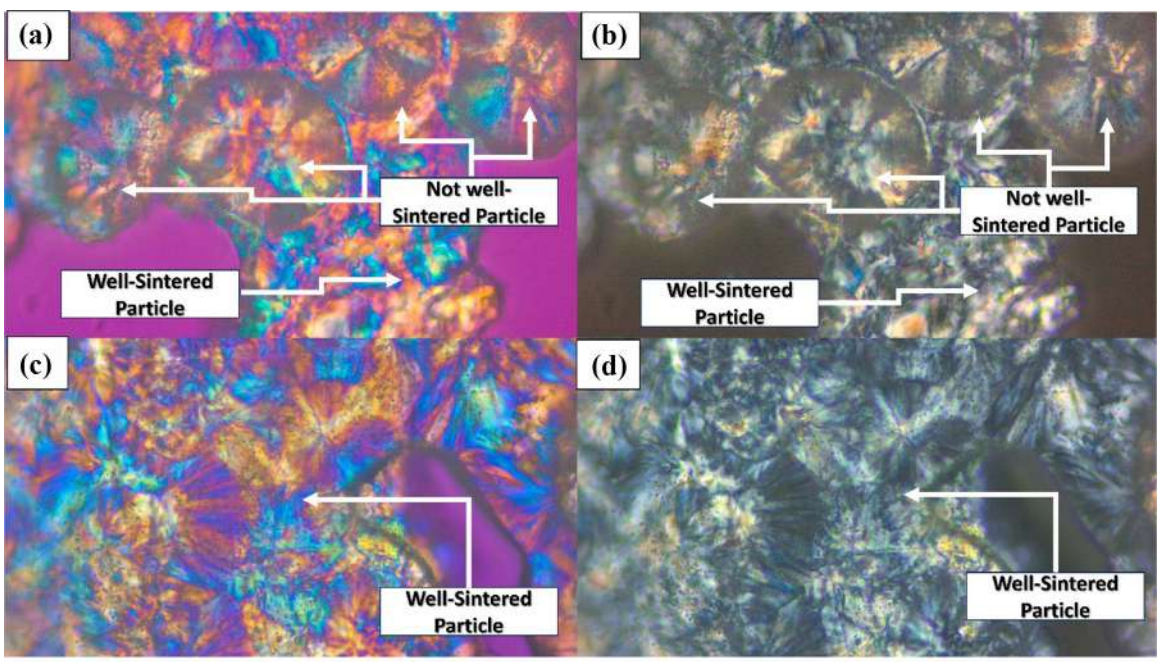

Source: Figure by authors'

Figure 16 Heatmaps of the porosity and gradient for specimens with different building directions and wall thicknesses

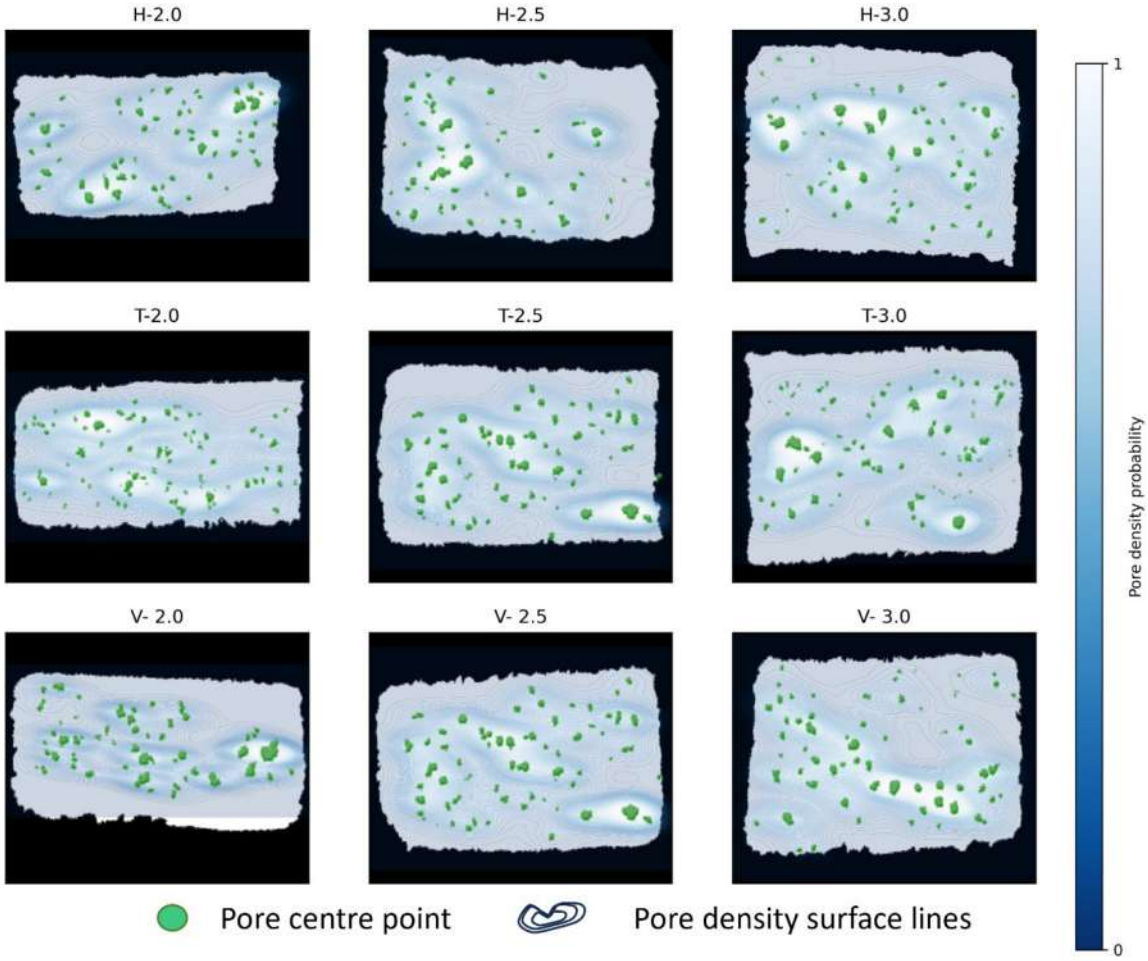

Source: Figure by authors'

build direction. Notably, the direction with the highest crystallinity (horizontal) demonstrated superior strength and ductility in fracture areas, suggesting that the specimen sintering layer area and cooling rate within the chamber significantly influence the type of fracture observed. This behaviour is also suggested by Alzyod and Ficzere (2023) and Griessbach *et al.* (2010), who indicated that the mass influences the residual stress of the part and the mechanical properties.

The stress–strain curves exhibit an initial increase in strain hardening, followed by a decrease in stress until it reaches the breaking point. This behaviour suggests that the ductile zone is first formed, and as the maximum stress is reached in the restraint zone, cracks appear that lead to the brittle zone. This phenomenon could be attributed to the low deformation observed in the vertical specimens after the point of maximum stress.

The presence of radial fracture marks in the delicate area suggests that the fracture originated from the surface of the specimen. This occurrence may be linked to the roughness of the sample because the partially functionalized particles act as stress concentrators, as noted by Caulfield *et al.* (2007) and Khan *et al.* (2021). Furthermore, the partially fused particles exhibited a distinct crystal morphology from the properly fused mass, indicating that crystal gradients on the surface could contribute to the development of external cracks. The generation of fractures can also be attributed to defects. Using the k-nearest neighbour machine learning model, we identified porosity trends that would have been undetectable to the naked eye. The model produced contour lines that revealed pore probability and colour maps that showed densities and trends in a geometric location in the cross-section. According to Kiani *et al.* (2020), defectology can affect fracture morphology. In our study, the pore probability map in the cross-sections of the specimens (Figure 16) indicates an increase in defect density from the centre to the corners of the specimens.

The brittle and ductile fracture rates are closely linked to the mechanical strength and Eab. Directions with greater Eab and UTS exhibited the most ductile zones. Researchers in the field, such as Caulfield *et al.*, 2007 (Ferreira *et al.*, 2020) and Hofland *et al.*, 2017 (Alzyod and Ficzere, 2023), have suggested that brittle fracture is related to low strength due to layer-by-layer construction in the vertical direction. Figure 11(a)–(b) illustrates that anisotropic crystalline conditions may result in low mechanical strength between

Figure 17 Mechanical, thermal and superficial behaviour on the build direction and thickness function

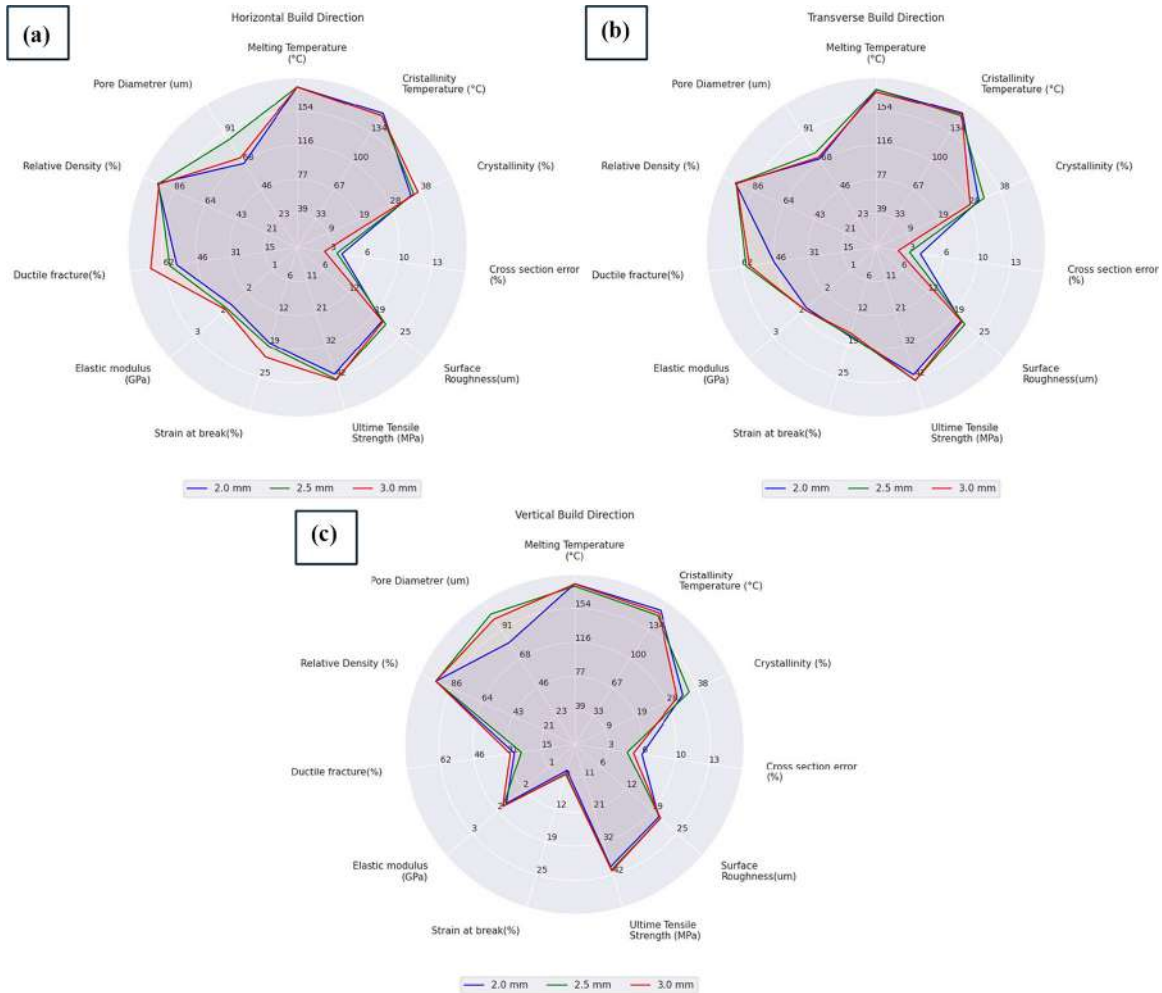

Source: Figure by authors'

sintering layers, thereby explaining the flatness of the fracture in the vertical direction. This observation was supported by SEM imaging conducted by El Magri *et al.* (2022). The differences in the ductile area shown in the ANOVA (Table 10) can be attributed to this fracture morphology, which indicates low interlayer fusion, resulting in a low ductile fracture zone with superficial fibrils. The depth of the fibrils is not solely dependent on the build direction, as shown in studies by Zehir *et al.*, 2024 (Garcia *et al.*, 2023), Tomanik *et al.* (2021) and the present research. The percentage of humidity and temperature of the assay, as reported by Seltzer *et al.* (2011) and Mielicki *et al.* (2014), can also affect the depth of the fibrils in the fractures. However, because the samples were under controlled conditions and at ambient temperature, the fibrils were deep in the ductile direction, with no changes in the FTIR spectra. Therefore, the fracture is not associated with the humidity or temperature of the sample.

The size of the ductile fracture zone depends on the degree of powder fusion, as suggested by Gümüs *et al.* (2018). The deformed spherulites suggest that sections containing fibrils underwent successful fusion between layers, with the horizontal build direction exhibiting the greatest ductility, followed by the transverse and vertical directions.

In terms of wall thickness, only roughness is significantly affected. However, this item is related to fracture. As the thickness increases, the ductile zone also increases, which is related to the increase in strength reported by Garcia *et al.* (2013) and Rodríguez *et al.* (2023).

5. Conclusions and recommendations

The build direction significantly impacts the properties of the sample. It affects its crystallinity, mechanical properties and ductile fracture rate, making it one of the most essential variables in fracture behaviour. The build direction with the highest deformation and ductile fracture area was horizontal, followed by the vertical and transverse directions. Microtomic slice fractography was used to analyse the crystalline behaviours of the samples, including the correct fusion of spherulites, partial fusion of particles, sintering lines and anisotropic crystalline conditions.

In the vertical direction, the brittle behaviour is related to anisotropic crystalline conditions associated with layer-by-layer construction that results in fractures perpendicular to the layers. The study also revealed that the fibrils were obtained after the deformation of the well-fused spherulites in the ductile section; for the brittle section, the spherulites fractured transversally.

This study used machine learning commands based on k-neighbours to generate a map showing trends of porosity concentrations and sizes in the centre of the specimen and at the corners. This map is a powerful tool for showing defectology behaviour in SLS-manufactured specimen sections. The study revealed that the fracture of the specimens nucleated from the surface was possibly due to the stress concentration produced by the partially fused particles on the surface and the porosity gradients near the corners.

This work can help identify the build direction through morphology, strength and fracture behaviour, providing tools for failure analysts to identify dual fractures in parts manufactured by SLS with 30:70 powder mixtures. It can also help understand how the build direction affects the fracture behaviour, which can be studied with higher test temperature conditions, wetting conditions and other surface parameters such as orange peel or surface treatments such as shot blasting.

References

Alzyod, H. and Ficzere, P. (2023), "Material-dependent effect of common printing parameters on residual stress and warpage deformation in 3D printing: a comprehensive finite element analysis study", *Polymers*, Vol. 15 No. 13, doi: 10.3390/polym15132893.

Amado-Becker, A., Ramos-Grez, J., José Yañez, M., Vargas, Y. and Gaete, L. (2008), "Elastic tensor stiffness coefficients for SLS nylon 12 under different degrees of densification as measured by ultrasonic technique", *Rapid Prototyping Journal*, Vol. 14 No. 5, pp. 260-270, doi: 10.1108/13552540810907929.

Amstutz, C., Weisse, B., Haeberlin, A., Burger, J. and Zurbuchen, A. (2022), "Inverse finite element approach to identify the post-necking hardening behavior of polyamide 12 under uniaxial tension", *Polymers (Basel)*, Vol. 14 No. 17, doi: 10.3390/polym14173476.

Amstutz, C., Weisse, B., Valet, S., Haeberlin, A., Burger, J. and Zurbuchen, A. (2021), "Temperature-dependent tensile properties of polyamide 12 for the use in percutaneous transluminal coronary angioplasty balloon catheters", *BioMedical Engineering OnLine*, Vol. 20 No. 1, pp. 1-20, doi: 10.1186/s12938-021-00947-8.

Balemans, C., Jaensson, N.O., Hulsen, M.A. and Anderson, P.D. (2018), "Temperature-dependent sintering of two viscous particles", *Additive Manufacturing*, Vol. 24, pp. 528-542, doi: 10.1016/j.addma.2018.09.005.

Cai, C., *et al.*, (2021), "Comparative study on 3D printing of polyamide 12 by selective laser sintering and multi jet fusion", *Journal of Materials Processing Technology*, Vol. 288, p. 116882, doi: 10.1016/j.jmatprotec.2020.116882.

Caulfield, B., McHugh, P.E. and Lohfeld, S. (2007), "Dependence of mechanical properties of polyamide components on build parameters in the SLS process", *Journal of Materials Processing Technology*, Vol. 182 Nos. 1/3, pp. 477-488, doi: 10.1016/j.jmatprotec.2006.09.007.

Charoo, N.A., *et al.*, (2020), "Selective laser sintering 3D printing–an overview of the technology and pharmaceutical applications", *Drug Development and Industrial Pharmacy*, Vol. 46 No. 6, pp. 869-877, doi: 10.1080/03639045.2020.1764027.

3D Systems (2020), "Rapid manufacturgin: SLS design guide-plastics", available at: www.3dsystems.com/resources/sls-plastics-design-guide (accessed 8 July 2024).

Douglas, C. (2001), "Montgomery", *Design and Analysis of Experiments*, Vol. 5.

El Magri, A., Bencaid, S.E., Vanaei, H.R. and Vaudreuil, S. (2022), "Effects of laser power and hatch orientation on final properties of PA12 parts produced by selective laser sintering", *Polymers (Basel)*, Vol. 14 No. 17, doi: 10.3390/polym14173674.

Fan, X., *et al.*, (2021), "Design, mechanical properties and energy absorption capability of graded-thickness triply periodic minimal surface structures fabricated by selective laser melting", *International Journal of Mechanical Sciences*, Vol. 204, doi: 10.1016/j.ijmecsci.2021.106586.

Ferreira, I., Melo, C., Neto, R., Machado, M., Alves, J.L. and Mould, S. (2020), "Study of the annealing influence on the mechanical performance of PA12 and PA12 fibre reinforced FFF printed specimens", *Rapid Prototyping Journal*, Vol. 26 No. 10, pp. 1761-1770, doi: 10.1108/RPJ-10-2019-0278.

Garcia, A., Espejo, E., Valsco, M. and Narvaez, C. (2023), "Mechanical properties of polyamide 12 manufactured by means of SLS: influence of wall thickness and build direction", *Materials Research Express*, Vol. 10 No. 10, doi: 10.1088/2053-1591/acf6f7.

Griessbach, S., Lach, R. and Grellmann, W. (2010), "Structure-property correlations of laser sintered nylon 12 for dynamic dye testing of plastic parts", *Polymer Testing*, Vol. 29 No. 8, pp. 1026-1030, doi: 10.1016/j.polymertesting.2010.09.010.

Gümüs, S., *et al.*, (2018), "Failure behavior of PA12 based SLS lattice structure with macroporosity", *MATEC Web of Conferences*, Vol. 188, doi: 10.1051/matecconf/201818803007.

Hashmi, A.W. and Meena, A. (2023), "Materials today: proceedings improving the surface characteristics of additively manufactured parts: a review", *Mater Today, Proc*, Vol. 81, pp. 723-738, doi: 10.1016/j.matpr.2021.04.223.

Hejmady, P., van Breemen, L.C.A., Hermida-Merino, D., Anderson, P.D. and Cardinaels, R. (2022), "Laser sintering of PA12 particles studied by in situ optical, thermal and X-ray characterisation", *Additive Manufacturing*, Vol. 52 No. January, p. 102624, doi: 10.1016/j.addma.2022.102624.

Hiramatsu, N., Haraguchi, K. and Hirakawa, S. (1983), "Study of transformations among alpha, gamma and gamma prime FORMS in NYLON 12 by X-RAY and DSC", *Jpn J Appl Phys Pt 1*, Vol. 22, No. 2, pp. 335-339.

Hofland, E.C., Baran, I. and Wismeijer, D.A. (2017), "Correlation of process parameters with mechanical properties of laser sintered PA12 parts", *Advances in Materials Science and Engineering*, Vol. 2017, doi: 10.1155/2017/4953173.

Jaksch, A., Cholewa, S. and Drummer, D. (2023), "Thin-Walled part properties in powder bed fusion of polymers–a comparative study on temperature development and part

performance depending on part thickness and orientation", *Journal of Manufacturing and Materials Processing*, Vol. 7 No. 3, doi: 10.3390/jmmp7030096.

Kelly, C.N., *et al.*, (2019), "Fatigue behavior of as-built selective laser melted titanium scaffolds with sheet-based gyroid microarchitecture for bone tissue engineering", *Acta Biomaterialia*, Vol. 94, pp. 610-626, doi: 10.1016/j.actbio.2019.05.046.

Khan, H., Sirin, M.T.B., Tarakci, G., Bulduk, M.E., Coskun, M. and Koc, E. (2021), "Improving the surface quality and mechanical properties of selective laser sintered PA2200 components by the vibratory surface finishing process", *SN Applied Sciences*, Vol. 3 No. 3, doi: 10.1007/s42452-021-04371-4.

Kiani, A., Khazaee, S., Badrossamay, M., Foroozmehr, E. and Karevan, M. (2020), "An investigation into thermal history and its correlation with mechanical properties of PA12 parts produced by selective laser sintering process", *Journal of Materials Engineering and Performance*, Vol. 29 No. 2, pp. 832-840, doi: 10.1007/s11665-020-04640-0.

Liu, Y., Zhu, L., Zhou, L. and Li, Y. (2019), "Microstructure and mechanical properties of reinforced polyamide 12 composites prepared by laser additive manufacturing", *Rapid Prototyping Journal*, Vol. 25 No. 6, pp. 1127-1134, doi: 10.1108/RPJ-08-2018-0220.

Ma, N. *et al.* (2020), "Crystal transition and thermal behavior of Nylon 12", *E-Polymers*, Vol. 20 No. 1, pp. 346-352, doi: 10.1515/epoly-2020-0039.

Majewski, C. and Hopkinson, N. (2011), "Effect of section thickness and build orientation on tensile properties and material characteristics of laser sintered nylon-12 parts", *Rapid Prototyping Journal*, Vol. 17 No. 3, pp. 176-180, doi: 10.1108/13552541111124743.

Martynková, G.S., *et al.*, (2021), "Polyamide 12 materials study of morpho-structural changes during laser sintering of 3d printing", *Polymers (Basel)*, Vol. 13 No. 5, doi: 10.3390/polym13050810.

Materialise (2024), "Design guidelines: PA 12 (sls)", available at: www.materialise.com/en/academy/industrial/design-am/pa12-sls

Mehdipour, F., Gebhardt, U. and Kästner, M. (2021), "Anisotropic and rate-dependent mechanical properties of 3D printed polyamide 12 – a comparison between selective laser sintering and multi jet fusion", *Results in Materials*, Vol. 11, p. 100213, doi: 10.1016/j.rinma.2021.100213.

Messiha, M., Frank, A., Heimink, J., Arbeiter, F. and Pinter, G. (2022), "Mechanisms of rapid fracture in PA12 grades", *Theoretical and Applied Fracture Mechanics*, Vol. 117, doi: 10.1016/j.tafmec.2021.103145.

Mielicki, C., Gronhoff, B. and Wortberg, J. (2014), "Effects of laser sintering processing time and temperature on changes in polyamide 12 powder particle size, shape and distribution", *AIP Conf Proc*, Vol. 1593, pp. 728-731, doi: 10.1063/1.4873880.

Nelson, J.A. and Rennie, A.E.W. (2015), "Effect of process conditions on temperature distribution in the powder bed during laser sintering of polyamide-12", *Journal of Thermal Engineering*, Vol. 1 No. 3, pp. 159-165, doi: 10.18186/jte.13739.

Ning, M., *et al.*, (2020), "Crystal transition and thermal behavior of nylon 12", *e-Polymers*, Vol. 20 No. 1, pp. 346-352.

Olakanmi, E.O. (2013), "Selective laser sintering/melting (SLS/SLM) of pure Al, Al-Mg, and Al-Si powders: effect of processing conditions and powder properties", *Journal of Materials Processing Technology*, Vol. 213 No. 8, pp. 1387-1405, doi: 10.1016/j.jmatprotec.2013.03.009.

Petzold, S., Klett, J., Schauer, A. and Osswald, T.A. (2019), "Surface roughness of polyamide 12 parts manufactured using selective laser sintering", *Polymer Testing*, Vol. 80 No. September, p. 106094, doi: 10.1016/j.polymertesting.2019.106094.

Proto3000 (2024), "Selective lase sintering (SLS) 3D printing design guidelines", available at: https://proto3000.com/service/3d-printing-services/materials/overview/designguidelines/sls-design-guidelines

Puttonen, T., Salmi, M. and Partanen, J. (2021), "Mechanical properties and fracture characterisation of additive manufacturing polyamide 12 after accelerated weathering", *Polymer Testing*, Vol. 104, p. 107376, doi: 10.1016/j.polymertesting.2021.107376.

Rodríguez, A.G., Mora, E.E., Velasco, M.A. and Tovar, C.A.N. (2023), "Mechanical properties of polyamide 12 manufactured by means of SLS: influence of wall thickness and build direction", *Materials Research Express*, Vol. 10 No. 10, doi: 10.1088/2053-1591/acf6f7.

Rosso, S., Meneghello, R., Biasetto, L., Grigolato, L., Concheri, G. and Savio, G. (2020), "In-depth comparison of polyamide 12 parts manufactured by multi jet fusion and selective laser sintering", *Additive Manufacturing*, Vol. 36, p. 101713, doi: 10.1016/j.addma.2020.101713.

Salmoria, G., Leite, V.J.L. and Paggi, R.A. (2009), "The microstructural characterisation of PA6/PA12 blend specimens fabricated by selective laser sintering", *Polymer Testing*, Vol. 28 No. 7, pp. 746-751, doi: 10.1016/j.polymertesting.2009.06.010.

Sasmita, F., Tarigan, T.Z.S., Judawisastra, H. and Priambodo, T.A. (2019), "Study of elastic modulus determination of polymers with ultrasonic method", *International Journal on Advanced Science, Engineering and Information Technology*, Vol. 9 No. 3, pp. 874-879, doi: 10.18517/ijaseit.9.3.4658.

Seltzer, R., de la Escalera, F.M. and Segurado, J. (2011), "Effect of water conditioning on the fracture behavior of PA12 composites processed by selective laser sintering", *Materials Science and Engineering: A*, Vol. 528 Nos 22/23, pp. 6927-6933, doi: 10.1016/j.msea.2011.05.045.

Sindinger, S., Kralovec, L.C., Tasch, D. and Schagerl, M. (2020), "Thickness dependent anisotropy of mechanical properties and inhomogeneous porosity characteristics in laser-sintered polyamide 12 specimens", *Addit Manuf*, Vol. 33, doi: 10.1016/j.addma.2020.101141.

Tasch, D., Mad, A., Stadlbauer, R. and Schagerl, M. (2018), "Thickness dependency of mechanical properties of laser-sintered polyamide lightweight structures", *Additive Manufacturing*, Vol. 23, pp. 25-33, doi: 10.1016/j.addma.2018.06.018.

Tomanik, M., Zmudzińska, M. and Wojtków, M. (2021), "Mechanical and structural evaluation of the PA12 desktop selective laser sintering printed parts regarding printing strategy", *3D Printing and Additive Manufacturing*,

Vol. 8 No. 4, pp. 271-279, doi: 10.1089/3dp.2020.0111.

V. A (2024), "Injection molding SPI surface finishes".

Van Hooreweder, B., Moens, D., Boonen, R. and Kruth, J.-P. (2013), "On the difference in material structure and fatigue properties of polyamide specimens produced by fused filament fabrication and selective laser sintering", *International Journal of Advanced Manufacturing Technology*, Vol. 111 Nos 1/2, pp. 93-107, doi: 10.1007/s00170-020-06026-x.

Van Hooreweder, B., De Coninck, F., Moens, D., Boonen, R. and Sas, P. (2010), "Microstructural characterisation of SLS-PA12 specimens under dynamic tension/compression excitation", *Polym Test*, Vol. 29 No. 3, pp. 319-326, doi: 10.1016/j.polymertesting.2009.12.006.

Varotsis, A.B. (2021), "Introduction to FDM 3D printing", 3dhubs, available at: www.3dhubs.com/knowledge-base/introduction-fdm-3d-printing

Wolf, M., Werner, J. and Drummer, D. (2020), "Weld seam morphology and bond strength of infrared and vibration welded SLS parts of polyamide 12 as a function of the layer build-up direction and the welding process", *Additive Manufacturing*, Vol. 36, p. 101451.

Yao, B., Li, Z. and Zhu, F. (2020), "Effect of powder recycling on anisotropic tensile properties of selective laser sintered PA2200 polyamide", *European Polymer Journal*, Vol. 141, p. 110093, doi: 10.1016/j.eurpolymj.2020.110093.

Yap, C.Y., *et al.*, (2015), "Review of selective laser melting: materials and applications", *Applied Physics Reviews*, Vol. 2 No. 4, doi: 10.1063/1.4935926.

Yu, G., Ma, J., Li, J., Wu, J., Yu, J. and Wang, X. (2022), "Mechanical and tribological properties of 3D printed polyamide 12 and SiC/PA12 composite by selective laser sintering", *Polymers (Basel)*, Vol. 14 No. 11, doi: 10.3390/polym14112167.

Zehir, B., Seyedzavvar, M. and Boğa, C. (2024), "Exploring mixed-mode fracture behavior and mechanical properties of selective laser sintered polyamide 12 components", *Rapid Prototyp J*, Vol. 30 No. 3, pp. 529-546, doi: 10.1108/RPJ-08-2023-0270.

Corresponding author

Alejandro Garcia Rodriguez can be contacted at: algarciar@unal.edu.co